


Two-dimensional scattering of sound at noncontinuum conditionsA. Manela ^{*}*Faculty of Aerospace Engineering, Technion—Israel Institute of Technology, Haifa 32000, Israel*Y. Ben-Ami *Wolfson Centre for Mathematical Biology, Mathematical Institute,
University of Oxford, Oxford OX2 6GG, United Kingdom*

(Received 17 February 2023; accepted 22 May 2023; published 12 June 2023)

We study the propagation and wall scattering of two-dimensional thermodynamic disturbances in a gas at noncontinuum conditions. Initial system perturbations are modeled as arbitrary (local) small-amplitude density or temperature inhomogeneities, prescribed in the vicinity of an impermeable specular or diffuse (isothermal) wall. The problem is analyzed in the free-molecular and ideal-flow limits, complemented by direct simulation Monte Carlo (DSMC) calculations at arbitrary rarefaction rates. Closed-form results are obtained for the collisionless and ideal-flow gas responses to impulse excitation, followed by comparisons between DSMC and limit-case predictions for the case of Gaussian perturbations. While the acoustic signal is subject only to a geometric two-dimensional decay and carries to large distances in the inviscid limit, it decays rapidly at high rarefaction rates due to the mechanism of molecular dispersion. Different from the identical gas responses to local compression and heating in the inviscid regime, qualitative differences are highlighted and analyzed in the free-molecular limit. The results additionally indicate lower pressure levels in an isothermal- compared with a specular-wall system, due to the exchange of gas-surface energy taking place in the former. Finally, the acoustic force acting on the solid surface is examined. Apart from an early-time repelling impact, peculiar late-time attraction is found in the case of gas heating excitation at high Knudsen numbers.

DOI: [10.1103/PhysRevFluids.8.063401](https://doi.org/10.1103/PhysRevFluids.8.063401)**I. INTRODUCTION**

Acoustic scattering of a point source at a solid surface has been studied extensively over the years as a model problem in continuum aeroacoustics [1]. The benchmark setup consists of a delta-function source placed in the vicinity of an impermeable wall, where specific treatments differ in details such as surface geometry and source properties. Subsequently, the point-source analysis has been applied in a Green's function approach for the computation of the acoustic field generated by the interaction of arbitrary sources with a given structure.

While the scattering problem has been treated in detail in the continuum regime, the effect of continuum breakdown has only been scarcely addressed. In gas flows, noncontinuum conditions prevail in acoustic setups where the length- or timescales become of the order of the molecular mean-free path or time, respectively. Starting in the 1950s and motivated by low-pressure and small-scale evolving technologies, investigations on sound propagation in rarefied gas flows have primarily focused on a one-dimensional setup of an infinite planar wall undergoing uniform small-amplitude mechanical [2–10] or thermal [9,11–14] excitations, and were recently complemented

*Corresponding author: amanela@technion.ac.il

by a two-dimensional study [15]. Other works have examined the propagation of acoustic waves in micro- and nano-channels [16–22], where the sources modeled mimic vibroacoustic sound generation, similar to an oscillating wall system. Following a different path of interest, several researchers have analyzed the propagation of flow-induced disturbances in rarefied gases. Specifically, setups with gas-fluidic thermal sources, having a fundamental relevance in the fields of microscale heat transfer [23,24] and ultrafast heating processes [25], have been considered. To this end, Logan [26], and then Berkovsky and Bashtovoi [27], focused on the propagation of thermal disturbances in a nonconfined gas, applying Grad’s moment equations and other model approximations of the Boltzmann equation. Later investigations have included the impact of boundaries reflections, yet were limited to the continuum limit of small Knudsen numbers [28,29]. The near-continuum gas response to local compression has been studied by Danforth and Long [30], who allowed large initial perturbations, but carried out numerical simulations in a nonconfined setup.

Recently, the one-dimensional propagation of small-amplitude thermodynamic disturbances at noncontinuum conditions has been considered in a wall-confined setup [31]. The work studied the system response to a temperature nonuniformity set at a given distance from an impermeable planar wall. In a sense, this may be considered as a one-dimensional simplification of the above-mentioned point-source diffraction problem. Observing the above, the objective of the present study is to extend existing studies by investigating the counterpart two-dimensional setup, where the source is localized in both parallel- and normal-to-wall directions. This problem, where the solid surface acts as a neutral scatterer and its interaction with an external near source is analyzed, is fundamentally different from most of the existing works on rarefied gas acoustics, where the surface acts as the system source of sound [2–22]. In what follows, we first consider the system response to planar impulse perturbations of the density and temperature fields, prescribed in the vicinity of an impermeable wall. Such inhomogeneities may occur due to gas local compression or heating, respectively. The problem is analyzed in both free-molecular and ideal-flow conditions to contrast the gas behavior in the two limits. Closed-form results are derived, highlighting the differences between system responses to local compression and heating in the free-molecular regime. The effect of wall conditions, varying between specular and fully diffuse (isothermal), is analyzed, and the acoustic force on the wall is computed. Remarkably, apart from the expected repelling force at short times, late-time attraction between the gas and the wall is observed at large rarefaction rates. Our scheme is then applied for the case of localized Gaussian excitations to enable comparison with direct simulation Monte Carlo (DSMC) calculations and capture the system response at intermediate rarefaction rates.

In the next section, the problem is stated. The free-molecular limit is considered in Sec. III and the ideal-flow regime is analyzed in Sec. IV. The DSMC scheme is described in Sec. V. Our results for the cases of impulse and Gaussian excitations are presented in Secs. VI and VII, respectively, followed by concluding comments in Sec. VIII. Technical details are relegated to the Appendices.

II. STATEMENT OF THE PROBLEM

A schematic of the problem is shown in Fig. 1. Consider a planar semi-infinite expanse of a monatomic gas set at $y^* > 0$ and confined by an infinite stationary solid boundary at $y^* = 0$ (hereafter, asterisks denote dimensional quantities). At time $t^* = 0$, the gas is placed at rest, with prescribed initial nonuniform distributions of its total density and temperature,

$$\rho_{\text{tot}}^*(0, x^*, y^*) = \rho_0^* + \varepsilon \rho_{\text{in}}^*(x^*, y^*) \quad \text{and} \quad T_{\text{tot}}^*(0, x^*, y^*) = T_0^* + \varepsilon T_{\text{in}}^*(x^*, y^*), \quad (1)$$

respectively. In Eq. (1), x^* is a coordinate measured parallel to the wall and $\varepsilon \ll 1$, so the system linearized response may be considered. Such scenarios may occur due to any small thermodynamic nonuniformities imposed by external disturbances of local compression or heating. To focus on two-dimensional effects, we consider initial disturbances that are confined to a narrow zone within the semiplane, located at a characteristic distance L^* from the boundary, as illustrated by the dashed circle in Fig. 1.

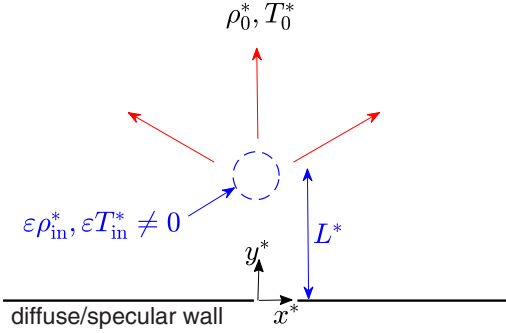


FIG. 1. Schematic of the problem. A semi-infinite gas expanse is confined by an infinite planar stationary wall. The gas uniform equilibrium density ρ_0^* and temperature T_0^* are locally perturbed at time $t^* = 0$. The characteristic distance between the local initial disturbances and the wall is L^* .

The work analyzes the combined effects of gas rarefaction, setup two-dimensionality, and surface properties on the propagation of gas initial disturbances and system relaxation. To this end, we compare between perfectly reflecting (specular) and fully diffuse (isothermal) wall surfaces, representing limit realizations of completely reflecting and accommodating boundaries, respectively. Diffuse scattering occurs over rough surfaces, where the colliding particles attain thermal equilibrium with the reflecting wall and evaporate accordingly. Specular interactions take place where the incident molecules collide with a solid surface and rebound elastically as if hitting a perfectly smooth wall. While none of these idealized scenarios exists in reality, it is commonly accepted that wall reflections from realistic surfaces may be described, in a variety of applications, as a combination of diffuse and specular interactions, as formulated in the prevalent Maxwell-type condition [32]. Since the combined diffuse-specular case merely superposes the above two limits, it is not discussed in detail hereafter.

Considering the problem formulation in the isothermal surface configuration, the wall temperature T_{wall}^* is assumed equal to the gas reference temperature, $T_{\text{wall}}^* = T_0^*$. In the other extreme of a specular surface, the gas response may be conveniently formulated by superposing the gas evolution in a counterpart unbounded domain (to be derived hereafter) with its symmetrical image about the surface location. In both isothermal and specular setups, a dimensionless description of the problem is obtained by scaling the position by the initial source-wall distance L^* , the velocity by the mean thermal speed of a gas molecule $U_{\text{th}}^* = \sqrt{2\mathcal{R}^*T_0^*}$ (with \mathcal{R}^* denoting the specific gas constant), and the time by the consequent timescale L^*/U_{th}^* . The density and temperature are normalized by ρ_0^* and T_0^* , respectively, and the pressure and stress-tensor components by $\rho_0^*\mathcal{R}^*T_0^*$. The nondimensional problem is then governed by the scaled initial disturbances $\rho_{\text{in}}(x, y)$ and $T_{\text{in}}(x, y)$, together with the reference Knudsen number

$$\text{Kn} = l^*/L^*, \quad (2)$$

marking the ratio between the mean-free path of a gas molecule l^* and the system characteristic length scale. Assuming a monatomic hard-sphere gas, the molecular mean free path is given by $l^* = m^*/(\sqrt{2\pi}\rho_0^*d^{*2})$, where m^* and d^* denote the molecular atomic mass and diameter, respectively [32].

The above diffuse- and specular-wall systems are considered in Secs. III and IV, where the limit cases of ballistic and ideal (inviscid) flow regimes are analyzed. Closed-form results are presented and discussed in Sec. VI for the case of impulse excitation. Comparison with DSMC predictions at arbitrary Knudsen numbers is carried out in Sec. VII for the case of Gaussian excitation.

III. FREE-MOLECULAR LIMIT

In the framework of gas kinetic theory and the unsteady two-dimensional configuration considered, the gas state is governed by the probability density function $f = f(t, x, y, \boldsymbol{\xi})$ of finding a gas

molecule with velocity about $\xi = (\xi_x, \xi_y, \xi_z)$ at a position near (x, y) at time t . At the linearized conditions assumed, we put

$$f(t, x, y, \xi) = F[1 + \varepsilon\phi(t, x, y, \xi)], \quad (3)$$

where $F = \pi^{-3/2} \exp[-\xi^2]$ denotes the nondimensional Maxwellian equilibrium distribution and $\phi(t, x, y, \xi)$ marks the probability perturbation function [33]. Assuming the Knudsen number to be large, we consider the collisionless two-dimensional unsteady Boltzmann equation for $\phi(t, x, y, \xi)$,

$$\frac{\partial\phi}{\partial t} + \xi_x \frac{\partial\phi}{\partial x} + \xi_y \frac{\partial\phi}{\partial y} = 0. \quad (4)$$

The equation is supplemented by the initial condition

$$\phi(0, x, y, \xi) = \phi_{\text{in}}(x, y, \xi), \quad (5)$$

which, in accordance with Eq. (1), takes the linearized form of deviation from equilibrium

$$\phi_{\text{in}}(x, y, \xi) = \rho_{\text{in}}(x, y) + T_{\text{in}}(x, y)(\xi^2 - 3/2). \quad (6)$$

The probability perturbation function is additionally subject to a far-field decay condition and a boundary condition imposed at the solid wall. For the case of a fully diffuse isothermal boundary, the latter takes the linearized half-range form

$$\phi^{(\text{iso})}(t, x, 0, \xi \cdot \hat{\mathbf{y}} > 0) = \rho_w(t, x), \quad (7)$$

where $\hat{\mathbf{y}}$ is a unit vector directed in the positive y direction (normal to the wall) and $\rho_w(t, x)$ is treated unknown. Considering a specular-wall setup, the probability perturbation function satisfies the symmetry condition

$$\phi^{(\text{spec})}(t, x, 0, \xi_x, \xi_y, \xi_z) = \phi^{(\text{spec})}(t, x, 0, \xi_x, -\xi_y, \xi_z). \quad (8)$$

The isothermal- and specular-wall setups are subsequently analyzed in Secs. III A and III B, respectively.

A. Isothermal wall

Considering a fully diffuse isothermal wall, the solution of Eq. (4) subject to the initial condition in Eq. (5) and boundary condition in Eq. (7) is

$$\phi^{(\text{iso})}(t, x, y, \xi) = \begin{cases} \rho_{\text{in}}(x - \xi_x t, y - \xi_y t) + T_{\text{in}}(x - \xi_x t, y - \xi_y t)(\xi^2 - 3/2), & \xi_y \leq y/t \\ \rho_w(t - y/\xi_y, x - y\xi_x/\xi_y), & \xi_y > y/t, \end{cases} \quad (9)$$

separating, at time t and location (x, y) , between particles which have $(\xi_y > y/t)$ or have not $(\xi_y \leq y/t)$ hit the wall since the initial $t = 0$ time. The wall function $\rho_w(t, x)$ is determined by imposing the linearized form of the impermeability condition at the wall. Applying Eq. (3), we obtain

$$v^{(\text{iso})}(t, x, 0) = \frac{1}{\pi^{3/2}} \int_{-\infty}^{\infty} \xi_y \phi^{(\text{iso})}(t, x, 0, \xi) \exp[-\xi^2] d\xi = 0. \quad (10)$$

Substituting Eq. (9) into Eq. (10), carrying the ξ_z integration and making the changes of variables $s = x - \xi_x t$ and $q = -\xi_y t$, we find

$$\begin{aligned} \rho_w(t, x) &= \frac{2}{\sqrt{\pi} t^3} \int_0^{\infty} q \exp\left[-\left(\frac{q}{t}\right)^2\right] \int_{-\infty}^{\infty} \left[\rho_{\text{in}}(s, q) + T_{\text{in}}(s, q) \left(\left(\frac{x-s}{t}\right)^2 + \left(\frac{q}{t}\right)^2 - 1 \right) \right] \\ &\quad \times \exp\left[-\left(\frac{x-s}{t}\right)^2\right] ds dq. \end{aligned} \quad (11)$$

Having fixed the solution for $\phi(t, x, y, \xi)$, appropriate quadratures over the velocity space yield expressions for the $O(\varepsilon)$ -scaled density $\rho^{(\text{iso})}(t, x, y)$, tangential velocity $u^{(\text{iso})}(t, x, y)$, normal velocity $v^{(\text{iso})}(t, x, y)$, and stress components deviations $P_{ij}^{(\text{iso})}(t, x, y)$ (with i and j being x, y , or z), as documented in Appendix A 1. The acoustic pressure and temperature perturbations are then given by

$$p^{(\text{iso})}(t, x, y) = \frac{2}{3}(P_{xx}^{(\text{iso})} + P_{yy}^{(\text{iso})} + P_{zz}^{(\text{iso})}) \quad \text{and} \quad T^{(\text{iso})}(t, x, y) = p^{(\text{iso})}(t, x, y) - \rho^{(\text{iso})}(t, x, y), \quad (12)$$

respectively, with the latter marking the linearized form of the gas equation of state.

B. Specular wall

The specular wall setup may be analyzed by superposing the gas response to initial disturbances in the absence of a boundary [$y \in (-\infty, \infty)$] with its symmetrical image about the surface location, such that the boundary condition Eq. (8) is identically satisfied. Making use of the linearized free-molecular solution in an unbounded domain [see Eqs. (4) and (5)],

$$\phi^{(\text{no-wall})}(t, x, y, \xi) = \phi_{\text{in}}(x - \xi_x t, y - \xi_y t, \xi), \quad (13)$$

the probability perturbation function in the case of a specular wall configuration [$y \in [0, \infty)$] is

$$\phi^{(\text{spec})}(t, x, y, \xi_x, \xi_y, \xi_z) = \begin{cases} \phi_{\text{in}}(x - \xi_x t, y - \xi_y t, \xi_x, \xi_y, \xi_z), & \xi_y \leq y/t \\ \phi_{\text{in}}(x - \xi_x t, -y + \xi_y t, \xi_x, -\xi_y, \xi_z), & \xi_y > y/t. \end{cases} \quad (14)$$

Substituting Eq. (14) into Eq. (3), the expressions for the acoustic fields follow by quadratures over the velocity space, as stated at the end of Sec. III A [with superscripts (iso) replaced by (spec)]. Specific expressions for the hydrodynamic fields in an unbounded plane are given in Appendix A 2. The specular-wall system response is obtained by superposition of the unbounded plane solution with its image about the boundary.

IV. CONTINUUM LIMIT

The problem at small Knudsen numbers may be analyzed based on a slip-flow continuum-limit model consisting of the continuum Navier-Stokes-Fourier (NSF) equations and respective wall conditions. Yet, considering the two-dimensional unsteady problem in hand, such calculation should require application of a fully numerical scheme that is not the focus of the present contribution. Additionally, since the DSMC method may be applied up to markedly low Knudsen [$\text{Kn} \sim O(10^{-3})$] numbers, it appears sufficient to analyze the ideal-flow (inviscid) regime as a contrast limit to the above free-molecular investigation. Advantageously, taking the $\text{Kn} \rightarrow 0$ limit simplifies the problem to an extent where it can be handled analytically. To start, since the order of equations is reduced (compared with the full NSF set), the boundary conditions for the tangential velocity and wall temperature cannot be satisfied. The problem is then identical with assuming a specular boundary, and the solution may be obtained through a superposition of the ideal-flow response in an unbounded domain with its symmetric reflection about $y = 0$. While this may be considered a standard problem in continuum acoustics, we could not identify a specific reference where it was previously considered, and present the analysis below and in Sec. VI B for completeness.

Adopting the scaling introduced in Sec. II, the linearized two-dimensional compressible Euler equations consist of the balances of mass

$$\frac{\partial \rho}{\partial t} + \frac{\partial u}{\partial x} + \frac{\partial v}{\partial y} = 0, \quad (15)$$

x -momentum

$$\frac{\partial u}{\partial t} = -\frac{1}{2} \left(\frac{\partial \rho}{\partial x} + \frac{\partial T}{\partial x} \right), \quad (16)$$

y-momentum

$$\frac{\partial v}{\partial t} = -\frac{1}{2} \left(\frac{\partial \rho}{\partial y} + \frac{\partial T}{\partial y} \right), \quad (17)$$

and energy

$$\frac{\partial T}{\partial t} = -(\gamma - 1) \left(\frac{\partial u}{\partial x} + \frac{\partial v}{\partial y} \right), \quad (18)$$

where the linearized form of the equation of state for an ideal gas, $p = \rho + T$, has been applied. Equations (15)–(18) are supplemented by the set of initial conditions,

$$\rho(0, x, y) = \rho_{\text{in}}(x, y), \quad T(0, x, y) = T_{\text{in}}(x, y) \quad \text{and} \quad u(0, x, y) = v(0, x, y) = 0, \quad (19)$$

together with the wall impermeability constraint,

$$v(t, x, 0) = 0. \quad (20)$$

Considering the infinite-plane setup with no boundaries [$x, y \in (-\infty, \infty)$], the ideal-flow problem is analyzed by taking the x - and y -Fourier transforms for each of the fields,

$$\bar{G}(t, k, \lambda) = \int_{-\infty}^{\infty} e^{-i\lambda y} \int_{-\infty}^{\infty} G^{(\text{no-wall})}(t, x, y) e^{-ikx} dx dy, \quad (21)$$

and applying to Eqs. (15)–(18). This yields a system of ordinary differential equations in time that may be recast as a Helmholtz-type equation for the density perturbation,

$$\frac{d^2 \bar{\rho}}{dt^2} + \omega^2 \bar{\rho} = \frac{\omega^2}{\gamma} [(\gamma - 1) \bar{\rho}_{\text{in}} - \bar{T}_{\text{in}}], \quad (22)$$

where $\omega = \sqrt{\gamma(k^2 + \lambda^2)}/2$ and the transformed form of the initial conditions in Eqs. (19) has been utilized. The solution for $\bar{\rho}(t, k, \lambda)$ is then

$$\bar{\rho}(t, k, \lambda) = \frac{1}{\gamma} (\bar{\rho}_{\text{in}} + \bar{T}_{\text{in}}) \cos(\omega t) + \frac{1}{\gamma} [(\gamma - 1) \bar{\rho}_{\text{in}} - \bar{T}_{\text{in}}], \quad (23)$$

followed by expressions for the transformed temperature

$$\bar{T}(t, k, \lambda) = \frac{\gamma - 1}{\gamma} (\bar{\rho}_{\text{in}} + \bar{T}_{\text{in}}) \cos(\omega t) - \frac{1}{\gamma} [(\gamma - 1) \bar{\rho}_{\text{in}} - \bar{T}_{\text{in}}], \quad (24)$$

velocity components

$$\bar{u}(t, k, \lambda) = -\frac{ik}{2\omega} (\bar{\rho}_{\text{in}} + \bar{T}_{\text{in}}) \sin(\omega t) \quad \text{and} \quad \bar{v}(t, k, \lambda) = -\frac{i\lambda}{2\omega} (\bar{\rho}_{\text{in}} + \bar{T}_{\text{in}}) \sin(\omega t), \quad (25)$$

and pressure

$$\bar{p}(t, k, \lambda) = (\bar{\rho}_{\text{in}} + \bar{T}_{\text{in}}) \cos(\omega t) \quad (26)$$

fields. The physical-domain solution in an unbounded plane is then calculated by taking the inverse Fourier transform,

$$G^{(\text{no-wall})}(t, x, y) = \frac{1}{4\pi^2} \int_{-\infty}^{\infty} e^{i\lambda y} \int_{-\infty}^{\infty} \bar{G}(t, k, \lambda) e^{ikx} dk d\lambda, \quad (27)$$

of the transformed perturbations and omitting the imaginary parts.

Having obtained the unbounded gas response, the calculation of the specular-wall system solution is carried out by superposing $G^{(\text{no-wall})}(t, x, y)$ with its symmetrical image about $y = 0$, similar to the discussion in Sec. III B. This ensures the vanishing of all odd (with respect to the y -molecular-velocity component) hydrodynamic moments at $y = 0$, as required by the specular

boundary condition. For given initial density and temperature perturbations, the solution may be computed in detail, as demonstrated in Secs. VI and VII.

V. NUMERICAL SCHEME: DSMC METHOD

The DSMC method, initially developed by Bird [34], is a stochastic particle-based method, routinely applied to simulate gas flows at noncontinuum conditions. In the present work, we make use of the DSMC scheme to validate the analytical ballistic- and ideal-flow limit solutions presented in Secs. III and IV, respectively, and explore the system behavior at arbitrary rarefaction rates. We accordingly adopt Bird's algorithm, together with the hard-sphere molecular interaction model [34], to simulate the gas state.

Each computation started at $t^* = 0$, where either initial temperature or density disturbances were imposed, in line with the problem formulation. For the temperature-driven case, the particles were assigned uniformly distributed random initial positions. Their velocities were chosen according to a Maxwellian distribution, with the temperature (governing the variance of particles' distribution) following the prescribed initial profile. For the density-driven case, the particles were assigned random uniformly distributed initial positions and a uniform-temperature Maxwellian distribution. Then, additional particles with positions distributed according to the prescribed density perturbation were added to satisfy the initial density condition. Each simulation followed in time until terminating at $t_{\text{sim}}^* \approx 3L^*/U_{\text{th}}^*$, which proved sufficient for the investigation of the interaction between the disturbance front [initially placed about $(x^*, y^*) = (0, L^*)$] and the $y^* = 0$ boundary. In line with problem formulation, the wall surface was assumed either specular or fully diffuse with prescribed uniform temperature T_0^* .

The size of the computational domain was set such that the signal does not reach (and is therefore not affected by) the virtual outer boundaries placed at $y_{\text{sim}}^* = 6L^*$ and $\pm x_{\text{sim}}^* = 6L^*$. The $(x^*, y^*) \in ([-x_{\text{sim}}^*, x_{\text{sim}}^*], [0, y_{\text{sim}}^*])$ domain was divided into ≈ 7000 cells and an additional division of each cell into collisional subcells was carried to comply with the mean-free-path limitations. A typical run consisted of $\approx 10^8$ particles, where ≈ 100 realizations were followed to sufficiently reduce the numerical noise. In line with the linearized problem formulation, a value of $\varepsilon = 0.1$ was taken, for which nonlinear effects proved to be negligible.

Inasmuch as the DSMC scheme was applied to support the limit-case analytical results, the accuracy of DSMC predictions may be supported by its agreement with the independent calculations at large and small Knudsen numbers. Thus, the close agreement at free-molecular and ideal-flow conditions, illustrated in Sec. VII, indicates the convergence of our DSMC calculations. Additionally, we performed numerical experiments in which we reduced the cell size and time step below their above-mentioned values. These had a negligible effect on the results, similarly supporting the convergence of our DSMC computations.

VI. IMPULSE RESPONSE

Applying the above schemes, our results may be obtained for arbitrary choices of the gas initial density and temperature perturbations, $\rho_{\text{in}}(x, y)$ and $T_{\text{in}}(x, y)$. In this section, results are presented for the case of an impulse input of either the density or temperature fields. Placing the initial disturbance at a unity distance from the wall, we set

$$\rho_{\text{in}}(x, y) = \delta(x)\delta(y - 1) \quad \text{or} \quad T_{\text{in}}(x, y) = \delta(x)\delta(y - 1), \quad (28)$$

where $\delta(\cdot)$ marks the Dirac Delta function. The cases of density and temperature perturbations are treated separately, i.e., with only one of the fields initially perturbed while the other is set uniform. The Delta-function formulation has the advantage of yielding closed-form results in the free-molecular and inviscid-flow limits, manifesting the system characteristic response to a point-localized two-dimensional input. Yet, the DSMC scheme could not be applied due to the

ambiguous representation of a Delta-function source in simulations. Numerical validation of our calculations is therefore deferred to Sec. VII, where a Gaussian input perturbation is discussed.

A. Free-molecular limit

Starting with the free-molecular limit for a specular-wall system, we substitute Eqs. (28) into Eqs. (A6) and (A7) and superpose all fields with their symmetric images about $y = 0$. Integrating and denoting

$$\begin{aligned}\Psi_{m,n}^{(\delta_\rho)}(t, x, y) &= \frac{x^n e^{-(x/t)^2}}{\pi t^{2+m+n}} \left\{ (y-1)^m \exp \left[-\left(\frac{y-1}{t}\right)^2 \right] + (y+1)^m \exp \left[-\left(\frac{y+1}{t}\right)^2 \right] \right\}, \\ \Psi_{m,n}^{(\delta_T)}(t, x, y) &= \frac{x^n e^{-(x/t)^2}}{\pi t^{2+m+n}} \left\{ (y-1)^m \exp \left[-\left(\frac{y-1}{t}\right)^2 \right] \left[\left(\frac{x}{t}\right)^2 + \left(\frac{y-1}{t}\right)^2 - 1 \right] \right. \\ &\quad \left. + (y+1)^m \exp \left[-\left(\frac{y+1}{t}\right)^2 \right] \left[\left(\frac{x}{t}\right)^2 + \left(\frac{y+1}{t}\right)^2 - 1 \right] \right\},\end{aligned}\quad (29)$$

we find for the free-molecular (FM) specular-wall response

$$\begin{aligned}\rho_{\text{FM}}^{(\text{spec})} &= \Psi_{0,0}^{(\delta_\rho)} + \Psi_{0,0}^{(\delta_T)}, & u_{\text{FM}}^{(\text{spec})} &= \Psi_{0,1}^{(\delta_\rho)} + \Psi_{0,1}^{(\delta_T)}, & v_{\text{FM}}^{(\text{spec})} &= \Psi_{1,0}^{(\delta_\rho)} + \Psi_{1,0}^{(\delta_T)}, \\ P_{xx,\text{FM}}^{(\text{spec})} &= \Psi_{0,2}^{(\delta_\rho)} + \Psi_{0,2}^{(\delta_T)}, & P_{yy,\text{FM}}^{(\text{spec})} &= \Psi_{2,0}^{(\delta_\rho)} + \Psi_{2,0}^{(\delta_T)},\end{aligned}\quad (30)$$

and

$$\begin{aligned}P_{zz,\text{FM}}^{(\text{spec})} &= \frac{1}{2} \Psi_{0,0}^{(\delta_\rho)} + \frac{e^{-(x/t)^2}}{2\pi t^2} \left\{ \exp \left[-\left(\frac{y-1}{t}\right)^2 \right] \left[\left(\frac{x}{t}\right)^2 + \left(\frac{y-1}{t}\right)^2 \right] \right. \\ &\quad \left. + \exp \left[-\left(\frac{y+1}{t}\right)^2 \right] \left[\left(\frac{x}{t}\right)^2 + \left(\frac{y+1}{t}\right)^2 \right] \right\},\end{aligned}\quad (31)$$

where the $\Psi_{m,n}^{(\delta_\rho)}$ and $\Psi_{m,n}^{(\delta_T)}$ parts in Eqs. (30) mark the separate contributions of the density $\rho_{\text{in}}(x, y) = \delta(x)\delta(y-1)$ and temperature $T_{\text{in}}(x, y) = \delta(x)\delta(y-1)$ perturbations to the acoustic fields, respectively. Similarly, $\Psi_{0,0}^{(\delta_\rho)}/2$ and the remaining part in Eq. (31) denote the separate contributions of the density and temperature perturbations to $P_{zz,\text{FM}}^{(\text{spec})}$, respectively. The acoustic pressure and temperature fields are obtained using the specular-wall counterparts of Eqs. (12), namely,

$$\begin{aligned}p_{\text{FM}}^{(\text{spec})}(t, x, y) &= \frac{2}{3} [P_{xx,\text{FM}}^{(\text{spec})} + P_{yy,\text{FM}}^{(\text{spec})} + P_{zz,\text{FM}}^{(\text{spec})}] = \frac{2}{3} \left[\Psi_{0,2}^{(\delta_T)} + \Psi_{0,2}^{(\delta_\rho)} + \Psi_{2,0}^{(\delta_T)} + \Psi_{2,0}^{(\delta_\rho)} + \frac{1}{2} \Psi_{0,0}^{(\delta_\rho)} \right. \\ &\quad \left. + \frac{e^{-(x/t)^2}}{2\pi t^2} \left\{ \exp \left[-\left(\frac{y-1}{t}\right)^2 \right] \left[\left(\frac{x}{t}\right)^2 + \left(\frac{y-1}{t}\right)^2 \right] \right. \right. \\ &\quad \left. \left. + \exp \left[-\left(\frac{y+1}{t}\right)^2 \right] \left[\left(\frac{x}{t}\right)^2 + \left(\frac{y+1}{t}\right)^2 \right] \right\} \right]\end{aligned}\quad (32)$$

and $T_{\text{FM}}^{(\text{spec})}(t, x, y) = p_{\text{FM}}^{(\text{spec})} - \rho_{\text{FM}}^{(\text{spec})}$, respectively. Counterpart expressions for the free-molecular isothermal-wall system response to an impulse input are tabulated in Appendix B.

B. Ideal-flow limit

Traversing to the other extreme of ideal-flow conditions, we substitute $\bar{\rho}_{\text{in}} = 1$ and $\bar{T}_{\text{in}} = 1$ for the above delta-function excitations [see Eqs. (28) and (21)] into Eqs. (23)–(26). Focusing on the

acoustic pressure in Eq. (26), the ideal-flow (IF) system response to a delta-function input in an unbounded domain is

$$p_{\text{IF}}^{(\text{no-wall})}(t, x, y) = \frac{1}{4\pi^2} \int_{-\infty}^{\infty} e^{i\lambda y} \int_{-\infty}^{\infty} \cos\left(\sqrt{\frac{\gamma(k^2 + \lambda^2)}{2}} t\right) e^{ikx} dk d\lambda, \quad (33)$$

for either density or temperature perturbations. Since the acoustic signal in the absence of boundaries propagates isotropically in all directions, we may, with no loss of generality, limit the calculation to a single direction, say $x = 0$. Additionally, changing to polar coordinates, $k = r \cos \theta$ and $\lambda = r \sin \theta$, we obtain

$$p_{\text{IF}}^{(\text{no-wall})}(t, 0, y) = \frac{1}{4\pi^2} \int_0^{\infty} r e^{irt\sqrt{\gamma/2}} \int_0^{2\pi} e^{iry \sin \theta} d\theta dr. \quad (34)$$

Applying a Bessel function identity [35], the θ integral is amenable to a closed-form expression, yielding

$$p_{\text{IF}}^{(\text{no-wall})}(t, 0, y) = \frac{1}{2\pi} \int_0^{\infty} \mathcal{J}_0(ry) e^{irt\sqrt{\gamma/2}} r dr, \quad (35)$$

where $\mathcal{J}_0(\cdot)$ denotes the Bessel function of the first kind and zeroth order. Numerical evaluation of the r integral in Eq. (35) indicates that $p_{\text{IF}}^{(\text{no-wall})}$ vanishes throughout the $(-\infty, \infty)$ y interval apart from sharp singularities at $y = \pm t\sqrt{\gamma/2}$. This result is further discussed in Sec. VIC, where the far-field ($y \gg 1$) evaluation of $p_{\text{IF}}^{(\text{no-wall})}$ is carried out. Once $p_{\text{IF}}^{(\text{no-wall})}(t, 0, y)$ is obtained, the specular-wall system response is calculated by superposing

$$p_{\text{IF}}^{(\text{spec})}(t, 0, y) = p_{\text{IF}}^{(\text{no-wall})}(t, 0, y - 1) + p_{\text{IF}}^{(\text{no-wall})}(t, 0, y + 1). \quad (36)$$

The entire two-dimensional acoustic field $p_{\text{IF}}^{(\text{spec})}(t, x, y)$ is computed based on Eq. (36) and the property of pressure isotropy in the absence of a boundary.

C. Results

Figure 2 compares the specular-wall free-molecular and ideal-flow system responses. The figure presents two-dimensional color maps of the acoustic pressure at times $t = 0.2, 1, \text{ and } 2$. In the free-molecular regime, the cases of density impulse [Figs. 2(d)–2(f)] and temperature impulse [Figs. 2(g)–2(i)] systems are shown. Figures 2(a)–2(c) show counterpart results in the inviscid limit, where the density- and temperature-driven pressure perturbations are identical [see Eq. (26)].

Starting with the inviscid response, we observe that the pressure disturbance at early times propagates as a circular discontinuity with radius $t\sqrt{\gamma/2} = t\sqrt{5/6}$. In each of Figs. 2(a)–2(c), the results have been rescaled by the pressure maximum value to restrict its upper bound to unity and thus regularize its singularity. Since the disturbance expands in the mean speed of sound ($=\sqrt{\gamma\mathcal{R}^*T_0^*}$ or $\sqrt{\gamma/2} = \sqrt{5/6}$ in mean-thermal-speed units), the signal is reflected at the wall at time $t = \sqrt{6/5}$. The pressure perturbation therefore retains its circular form in both Figs. 2(a) (for $t = 0.2$) and 2(b) (for $t = 1$). The impact of wall reflection is observed in Fig. 2(c), manifested by the lower circular arc emanating from the image source positioned at $(x, y) = (0, -1)$. While the singular character of the inviscid (nondiffusing) wave propagation carries to later times, its pointwise amplitude decays, as characteristic of two-dimensional acoustic sources and quantitated below [see Eq. (39) *et seq.*].

Comparing between the inviscid and free-molecular acoustic fields in Fig. 2, several fundamental differences are observed. At first, the free-molecular signal is not confined to a thin circular curve but spreads over a large portion of the (x, y) plane presented. Additionally, the pressure levels at large Knudsen numbers decay rapidly with time and the signal propagates in practice to only a few length scales away from the source. The time of signal initial impact at the boundary appears earlier in the free-molecular than in the ideal-flow case. Different from the latter, the signal impact time cannot be precisely defined in the free-molecular regime. Rather, the interaction of the acoustic disturbance

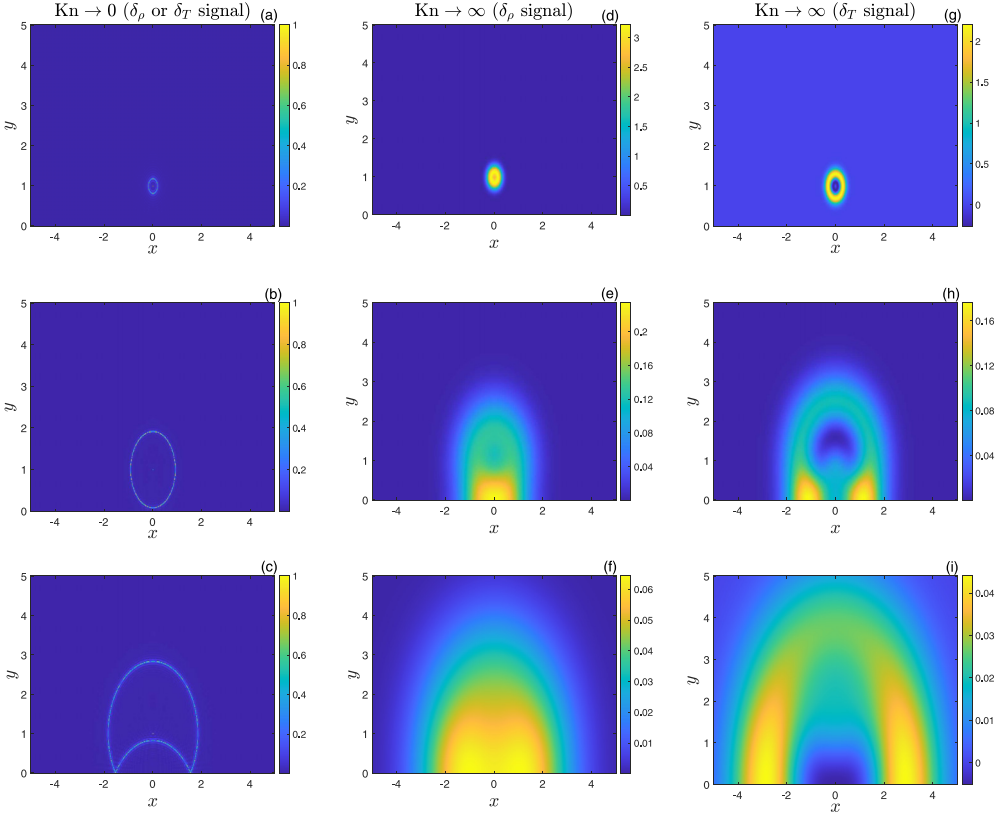


FIG. 2. The specular-wall ideal-flow [$\text{Kn} \rightarrow 0$, (a)–(c)] and free-molecular [$\text{Kn} \rightarrow \infty$, (d)–(i)] acoustic pressures in response to impulse perturbations of the density field [(d)–(f)], temperature field [(g)–(i)], and the density or the temperature [(a)–(c)]. Presented are two-dimensional color maps of the ε -scaled acoustic pressure at times $t = 0.2$ [(a), (d), (g)], $t = 1$ [(b), (e), (h)], and $t = 2$ [(c), (f), (i)]. In [(a)–(c)], the results have been scaled by their maximum values, to regularize pressure singularity.

with the wall at large Knudsen numbers may be described as a continual process, reflecting the molecular interaction of different noncolliding particles originating at the source and hitting the surface with varying speeds at different times. Since the free-molecular interaction of the acoustic disturbance with the wall occurs at all times, and is affected at early time by fast molecules that travel at speeds larger than the speed of sound, it is observed that the information on the initial perturbation reaches the wall earlier than in the continuum limit.

The fast time decay of the free-molecular signal, illustrated by the low $O(10^{-2})$ pressure levels at $t = 2$ [see Figs. 2(f) and 2(i)], reflects the strong effect of molecular dispersion on sound propagation at large Knudsen numbers. Comparing between the density-driven [Figs. 2(d)–2(f)] and temperature-driven [Figs. 2(g)–2(i)] responses, we observe that somewhat lower pressure amplitudes characterize the latter. Additionally, different propagation patterns are seen in the two cases. Here, at late times and with increasing distance from the source, the temperature-driven pressure exhibits multiple extremal points before eventual decay, whereas the density-driven signal is characterized by a single maximum that travels away from the initial excitation point with increasing time.

To quantify the above observations and gain further insight into the differences between the system responses in the ballistic and continuum regimes, we inspect the respective far-field ($|x| \gg 1$ or $y \gg 1$) descriptions of the acoustic pressure. The closed-form expressions obtained in Sec. VIA

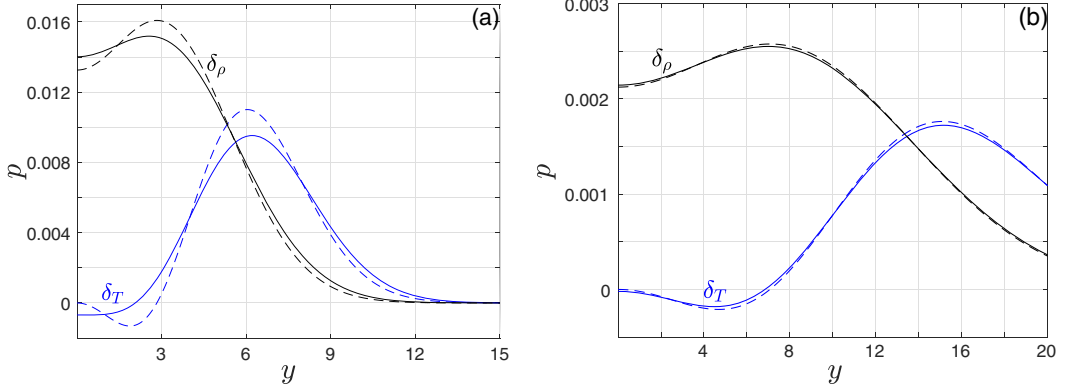


FIG. 3. The free-molecular acoustic pressure in response to an impulse excitation for a specular wall system at times $t = 4$ (a) and $t = 10$ (b). The figures show y variations of the pressure perturbation at $x = 0$ for the cases of initial density (black lines) and temperature (blue curves) impulse inputs. The solid and dashed lines present the full solution and far-field approximations, respectively.

for the free-molecular fields may be readily simplified to obtain the far-field behavior. In the ideal-flow regime, the far-field pressure is estimated through asymptotic evaluation of the integral in Eq. (35).

Starting with the free-molecular acoustic pressure in Eq. (32) and taking $R = \sqrt{x^2 + y^2} \gg 1$, we find

$$\begin{aligned}
 p_{\text{FM}}^{(\delta_\rho, \text{spec})} &\approx \frac{4}{3\pi t^2} \left[\left(\frac{R}{t} \right)^2 + \frac{1}{2} \right] \exp \left[- \left(\frac{R}{t} \right)^2 \right] \quad \text{and} \\
 p_{\text{FM}}^{(\delta_T, \text{spec})} &\approx \frac{4R^2}{3\pi t^4} \left[\left(\frac{R}{t} \right)^2 - \frac{1}{2} \right] \exp \left[- \left(\frac{R}{t} \right)^2 \right]
 \end{aligned} \tag{37}$$

for the far-field acoustic pressure in response to the density and temperature Delta-function perturbations, respectively. Thus, both fields exhibit an exponential decay with the square distance from the source. Yet, the decay is nonmonotonic, containing a maximum at $R/t \approx 2^{-1/2}$ in the density-driven case, and minimum and maximum values at $R/t \approx \sqrt{5 - 17^{1/2}}/2$ and $R/t \approx \sqrt{5 + 17^{1/2}}/2$, respectively, in the temperature-driven field. These results are illustrated in Fig. 3, where the y variation of the free-molecular acoustic pressure along $x = 0$ is plotted at times $t = 4$ [Fig. 3(a)] and $t = 10$ [Fig. 3(b)] and the far-field approximations in Eqs. (37) are compared with their exact counterparts in Eq. (32). The far-field approximations improve with increasing time, where the acoustic pressure turns smaller and its extremal values occur further away from the source. The different decay patterns in the density- and temperature-driven pressure variations qualitatively agree with the results in Fig. 2, showing a minimum-maximum variation of the temperature-driven signal in Figs. 2(h) and 2(i), in variance from the single maximum behavior depicted in Figs. 2(e) and 2(f).

To consider the far-field system response in the inviscid $\text{Kn} \rightarrow 0$ limit, we substitute the large-argument approximation for the Bessel function [35],

$$\mathcal{J}_0(ry) = \sqrt{\frac{2}{\pi ry}} \sin \left(ry + \frac{\pi}{4} \right) + O((ry)^{-3/2}),$$

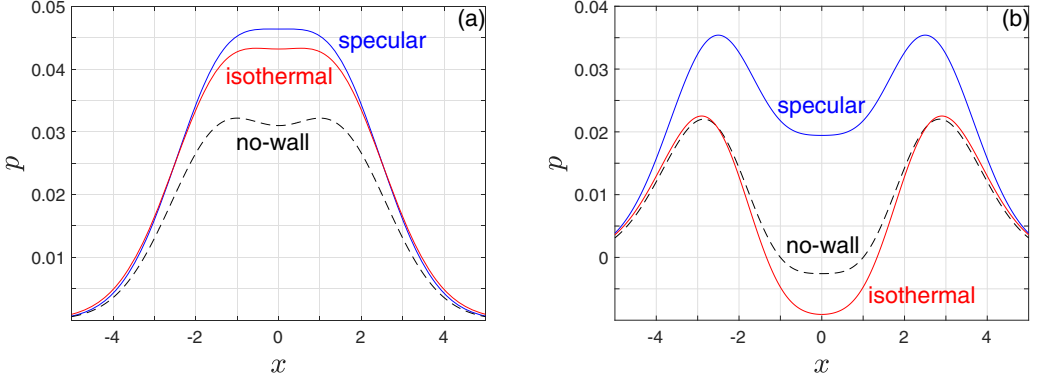


FIG. 4. Effect of surface boundary conditions on the acoustic pressure at time $t = 2$ and distance $y = 2$ from the surface. (a) and (b) present the pressure perturbation in response to density and temperature impulse excitations, respectively. The blue and red lines show results for specular- and isothermal-wall systems and the dashed black lines depict the pressure variation in the absence of a wall.

into the right-hand side of Eq. (35). The leading-order approximation for the acoustic pressure in the absence of a boundary may then be evaluated by

$$p_{\text{IF}}^{(\text{no-wall})}(t, 0, y \gg 1) \approx \frac{1}{2\pi \sqrt{2y}|y - t\sqrt{\gamma/2}|^{3/2}}. \quad (38)$$

The far-field specular-wall response is calculated using Eq. (36), yielding

$$p_{\text{IF}}^{(\text{spec})}(t, 0, y \gg 1) \approx \frac{1}{\pi \sqrt{2y}|y - t\sqrt{\gamma/2}|^{3/2}}. \quad (39)$$

Similar to Eq. (36), the far $p_{\text{IF}}^{(\text{spec})}(t, x, y)$ distribution is obtained using Eq. (39) and the property of pressure isotropy in the absence of a wall.

In line with the results in Figs. 2(a)–2(c), the ideal-flow far acoustic field in Eq. (39) exhibits a singular behavior at $y = t\sqrt{\gamma/2}$, namely, at a distance traveled by the disturbance at time t via propagation in the scaled speed of sound $\sqrt{\gamma/2}$. This is coupled with a square-root geometric decay of the signal [$\propto y^{-1/2}$ in Eq. (39)], preserving the system acoustic power as common in inviscid two-dimensional problems. Comparing with Eqs. (37) and Fig. 3, it is noted again that the free-molecular and ideal-flow fields qualitatively differ in both amplitude and pattern. As in Fig. 2, while the $\text{Kn} \rightarrow 0$ response is identical for both density- and temperature-driven signals, it varies between the two in the ballistic limit.

Figure 4 illustrates the effect of wall surface conditions on the system response. The figure presents x -variations of the acoustic pressure at time $t = 2$ and a distance $y = 2$ from the boundary for the density- [Fig. 4(a)] and temperature-impulse-excited [Fig. 4(b)] systems. Each figure compares between the specular- (blue lines) and isothermal- (red curves) wall signals. The reference acoustic pressure in the absence of a wall is presented by the dashed black curves. It is first observed that the specular- and isothermal-wall systems show similar qualitative behaviors, following the flat-peak [in Fig. 4(a), for the density-driven case] and double-peak [in Fig. 4(b), for the heating-excited response] x -variations in Figs. 2(f) and 2(i), respectively. Yet, the specular-wall signal is systematically larger in amplitude than the isothermal due to the exchange of energy between the gas and the surface, taking place in the latter and missing in the former. It may therefore be deduced that the specular-wall system, while simplifying the analysis, retains the qualitative characteristics of the isothermal-wall response, and can serve as an upper bound measure for the wall effect. Expectedly, both signals are larger in amplitude than the counterpart no-wall pressure, which propagates isotropically in all directions with no surface reflection.

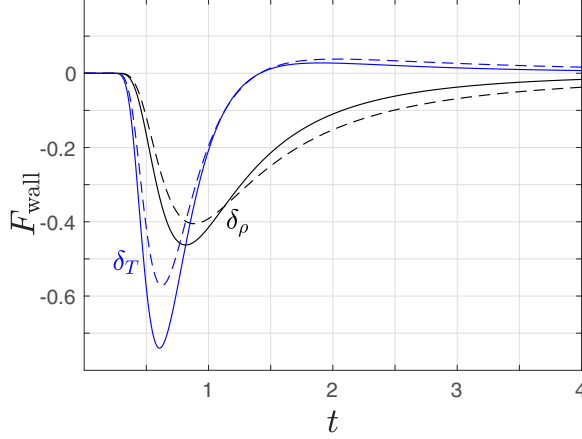


FIG. 5. Time variations of the free-molecular acoustic force on a specular (solid lines) and an isothermal (dashed curves) wall in response to an impulse perturbation of the density (black curves) and the temperature (blue lines) fields.

The discussion of the system response to an impulse is concluded by considering the normal acoustic force (per unit length) acting on the solid surface, given by

$$F_{\text{wall}}(t) = - \int_{-\infty}^{\infty} P_{yy}(t, x, 0) dx. \quad (40)$$

No net shear force is induced at the wall due to problem symmetry. In the free-molecular limit and for a specular-wall system, substituting $P_{yy}^{(\text{spec})}$ in Eqs. (30) into Eq. (40) and integrating, we obtain

$$F_{\text{wall,FM}}^{(\delta_\rho, \text{spec})}(t) = -\frac{2}{\sqrt{\pi}t^3} e^{-1/t^2} \quad \text{and} \quad F_{\text{wall,FM}}^{(\delta_T, \text{spec})}(t) = -\frac{2}{\sqrt{\pi}t^3} \left[\left(\frac{1}{t} \right)^2 - \frac{1}{2} \right] e^{-1/t^2} \quad (41)$$

for the cases of density and temperature input impulses, respectively. Following a similar procedure in the free-molecular isothermal-wall case, we find

$$F_{\text{wall,FM}}^{(\delta_\rho, \text{iso})}(t) = -\frac{1}{t^2} \left(\frac{1}{\sqrt{\pi}t} + \frac{1}{2} \right) e^{-1/t^2} \quad \text{and} \quad F_{\text{wall,FM}}^{(\delta_T, \text{iso})}(t) = -\frac{1}{t^2} \left(\frac{1}{\sqrt{\pi}t} + \frac{1}{2} \right) \left[\left(\frac{1}{t} \right)^2 - \frac{1}{2} \right] e^{-1/t^2}. \quad (42)$$

In the ideal-flow limit, we substitute $P_{yy} = p_{\text{IF}}^{(\text{spec})}$ in both density- and temperature-driven cases. Using Eq. (36) together with Eq. (33) in Eq. (40) and applying the Delta-function identity $\delta(s) = \int_{-\infty}^{\infty} \exp[isz] dz$, we find

$$F_{\text{wall,IF}}^{(\text{spec})}(t) = -\delta(t\sqrt{\gamma/2} - 1), \quad (43)$$

remanifesting the propagation of the initial discontinuity at inviscid flow conditions and its impact at the surface at the time of signal reflection at the wall, $t^* = L^*/(\gamma\mathcal{R}^*T_0^*)^{1/2}$. This is markedly different from the smoothly varying and infinitely weaker force in the collisionless limit, given by Eqs. (41) and (42).

The results for the free-molecular acoustic force are presented in Fig. 5. Both temperature- and density-driven forces vanish at short ($t \lesssim 0.3$) times, when the signal enforced at $y = 1$ has not yet affected the surface. At a later time, a maximum repelling force is observed in the two setups, caused by the interaction of the signal front with the boundary. Focusing on the specular-wall configuration, the maximum force in the density-driven case occurs at a later time ($t = \sqrt{2/3} \approx 0.817$) and with a lower amplitude ($F^{(\delta_\rho, \text{spec})} \approx -0.463$) compared with the temperature-perturbed system (where

$F^{(\delta_T, \text{spec})} \approx -0.740$ at $t = [(6 - 2\sqrt{6})/3]^{1/2} \approx 0.606$). Indeed, it is plausible that the gas particles in the thermally excited system obtain higher mean speeds, and thus arrive at the surface at earlier times and with a larger impact. Comparing between the specular (solid lines) and isothermal (dashed curves) force signals, the latter follows similar trends, yet exhibits lower repulsion maxima. As in Fig. 4, this is attributed to the transfer of thermal energy between the gas and the boundary, occurring in the isothermal-surface case and missing in the specular-wall system.

Remarkably, the acoustic force in the thermally driven system shows a slight attraction force ($F_{\text{wall}} > 0$) at late times, reaching a maximum of $F^{(\delta_T, \text{spec})} \approx 0.028$ at time $t = [(6 + 2\sqrt{6})/3]^{1/2} \approx 1.906$. A similar result is observed in the isothermal-wall system, while no such trend is viewed in the density-impulse case. Reverting to the expression for the normal wall stress $P_{yy}(t, x, 0)$ in the specular-wall system [appearing in the integrand for $F_{\text{wall}}(t)$ in Eq. (40)], we apply Eqs. (30) to find

$$P_{yy, \text{FM}}^{(\delta_\rho, \text{spec})}(t, x, 0) = \frac{2}{\pi t^4} e^{-(x^2+1)/t^2} \quad \text{and} \quad P_{yy, \text{FM}}^{(\delta_T, \text{spec})}(t, x, 0) = \frac{2}{\pi t^4} e^{-(x^2+1)/t^2} \left(\frac{x^2+1}{t^2} - 1 \right). \quad (44)$$

Thus, while $P_{yy, \text{FM}}^{(\delta_\rho, \text{spec})}(t, x, 0)$ is invariantly positive, yielding a repelling force at all times for a density-perturbed system, $P_{yy, \text{FM}}^{(\delta_T, \text{spec})}(t, x, 0)$ becomes negative through the $-\sqrt{t^2-1} < x < \sqrt{t^2-1}$ portion of the wall for $t > 1$. This, in turn, leads to a positive attraction force at late times. To trace the origin of the change in sign in $P_{yy, \text{FM}}^{(\delta_T, \text{spec})}(t, x, 0)$, we recall that [cf. Eq. (A1)]

$$P_{yy}^{(\delta_T, \text{spec})}(t, x, 0) = \pi^{-3/2} \int_{-\infty}^{\infty} \xi_y^2 \phi^{(\delta_T, \text{spec})}(t, x, 0, \xi) e^{-\xi^2} d\xi, \quad (45)$$

where [cf. Eq. (14) together with Eqs. (6) and (28)]

$$\phi^{(\delta_T, \text{spec})}(t, x, 0, \xi) = \delta(x - \xi_x t) \delta(|\xi_y|t - 1) (\xi^2 - 3/2). \quad (46)$$

Hence, it is the change in sign in $\xi^2 - 3/2$ (and, specifically, the $-3/2$ term within) in the probability perturbation function that leads to the late-time attraction force. Occurring for particles with $|\xi| < \sqrt{3/2}$, this change is attributed to the lower amount of slower particles, compared to equilibrium conditions, that arrive at the boundary at later times. Being fewer in number, their total impact is in the production of a positive attraction force. No similar mechanism is observed in the density-driven case, where the imposed increase in gas density leads to an invariantly positive value of $\phi^{(\delta_\rho, \text{spec})}(t, x, 0, \xi)$.

VII. GAUSSIAN EXCITATION

While the system response to an impulse was discussed in detail in the collisionless and ideal-flow regimes, DSMC analysis of the gas behavior at intermediate Knudsen numbers requires the consideration of a continuous initial distribution. To this end, we analyze the system response to a two-dimensional Gaussian excitation of either the density or the temperature,

$$\rho_{\text{in}}(x, y) = \exp[-\alpha((x-1)^2 + y^2)] \quad \text{or} \quad T_{\text{in}}(x, y) = \exp[-\alpha((x-1)^2 + y^2)], \quad (47)$$

marking a smooth initial disturbance peaked at $(x, y) = (0, 1)$. A value of $\alpha = 20$ ($\gg 1$) is taken to consider a relatively localized initial perturbation that decays sharply about its peak and does not interact with the $y = 0$ surface at $t = 0^+$. Additionally, a Gaussian distribution may be related to the above-studied impulse input via the limit $\delta(s) = \lim_{\alpha \rightarrow \infty} \sqrt{\alpha/\pi} \exp[-\alpha s^2]$. In this respect, while the Gaussian signal may be considered qualitatively similar to an impulse input, it is lower in amplitude and not as focused as the impulse, leading to quantitatively different results. These differences may be viewed by comparing between the pressure fields and acoustic forces presented below with those in Figs. 2 and 5 at large and small Knudsen numbers.

In what follows, the free-molecular and inviscid approximations are compared with DSMC predictions at finite Knudsen numbers to test their applicability and breakdown. Based on the scaling

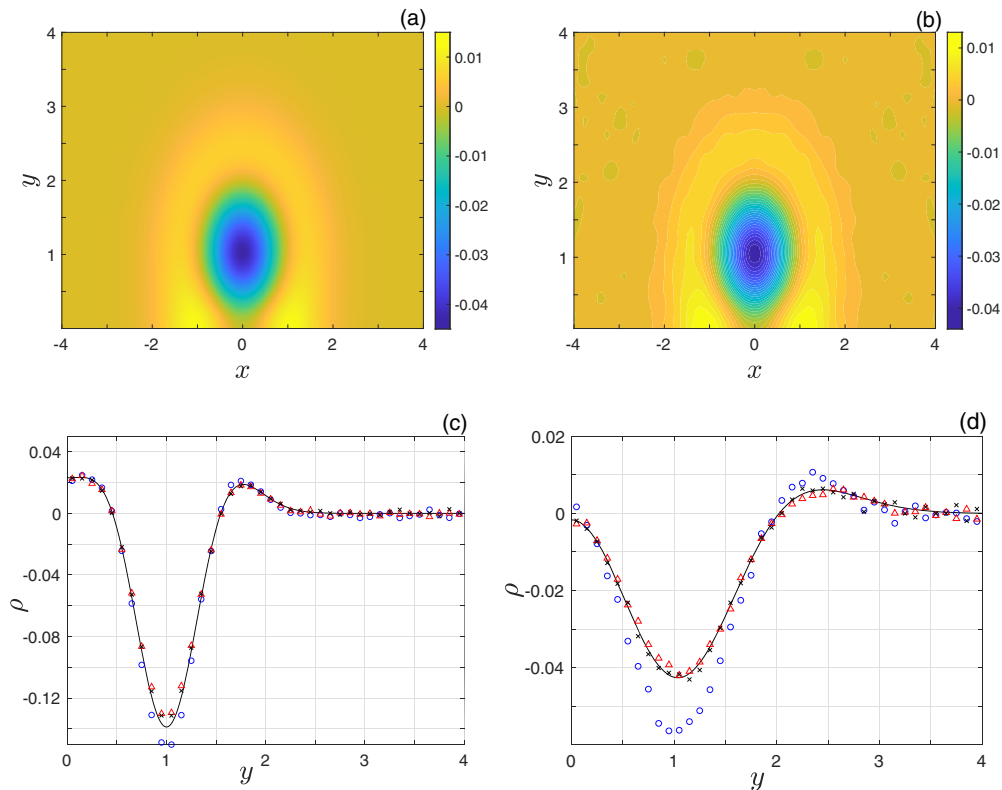


FIG. 6. The density perturbation in response to a Gaussian temperature excitation for a specular-wall system. (a), (b) Density color maps at time $t = 1$ for $\text{Kn} \rightarrow \infty$ (analytical solution) and $\text{Kn} = 10$ (DSMC), respectively. (c), (d) y variations along $x = 0$ of the density at times $t = 0.5$ and $t = 1$, respectively. The solid lines mark the free-molecular solution and the red triangles, black crosses, and blue circles denote DSMC results at $\text{Kn} = 10, 1$ and 0.1 , respectively.

introduced in Sec. II, the expected flow regime may be determined by the ratio between the Knudsen number and the time elapsed since the initiation of flow disturbance. To this end, collisionless flow conditions should prevail at $t/\text{Kn} \ll 1$, whereas the continuum limit approximation is expected valid at $t/\text{Kn} \gg 1$. In between, the intermediate regime should take place and follow the transition described below. To make presentation concise, our results mainly focus on the case of thermal system excitation.

Figure 6 compares between the free-molecular and DSMC predictions for a thermally excited specular-wall system. The figure presents two-dimensional color maps for the collisionless [Fig. 6(a)] and DSMC $\text{Kn} = 10$ [Fig. 6(b)] density perturbations at $t = 1$, together with pointwise y variations of the free-molecular and DSMC $\text{Kn} = 10, 1$ and 0.1 solutions at times $t = 0.5$ [Fig. 6(c)] and $t = 1$ [Fig. 6(d)]. At time $t = 1$, the acoustic signal is characterized by a strong interaction between the disturbance front and the boundary, captured by Figs. 6(a) and 6(b). While the DSMC-predicted field in Fig. 6(b) is inevitably noisy, its close agreement with the collisionless-regime result in Fig. 6(a) is evident. The detailed comparison in Figs. 6(c) and 6(d) further validates the effectiveness of the free-molecular description. Notably, at $t = 0.5$ [presented in Fig. 6(c)], the collisionless field matches with both $\text{Kn} = 10$ and 1 DSMC predictions for all y , while departing from the $\text{Kn} = 0.1$ field only about $y \approx 1$. With increasing time, the agreement of the $\text{Kn} \rightarrow \infty$ result with $\text{Kn} = 0.1$ predictions breaks down at earlier times, manifesting the growing impact of

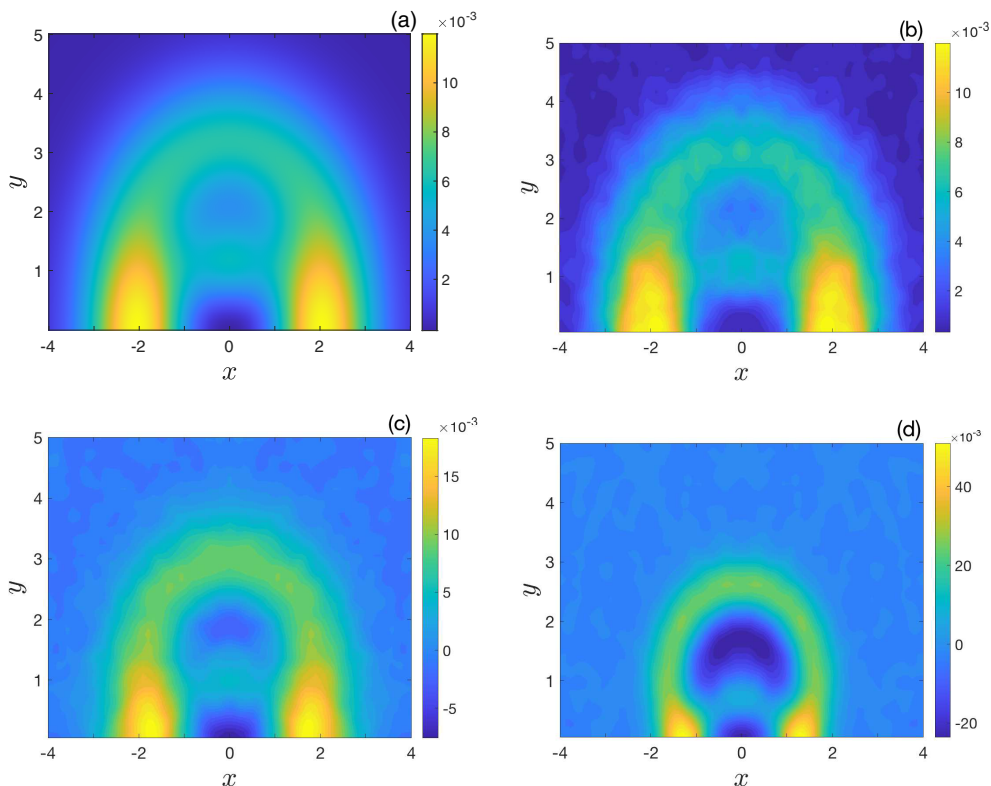


FIG. 7. Effect of gas rarefaction on the acoustic pressure in response to a Gaussian temperature excitation in a specular-wall system. Presented are two-dimensional color maps at $t = 1.5$ with (a) $\text{Kn} \rightarrow \infty$, (b) $\text{Kn} = 1$, (c) $\text{Kn} = 0.1$, and (d) $\text{Kn} = 0.01$.

molecular collisions. As stated above, it is expected that the collisionless description remains valid at small enough values of t/Kn , where the time elapsed since system excitation is short compared with the mean free time. In practice, the results indicate that the ballistic description remains valid up to times that are of the order of the mean free time, $t \approx \text{Kn}$, and even slightly later.

Having demonstrated the applicability of the free-molecular solution, Fig. 7 presents the overall effect of gas rarefaction on the acoustic field. Fixing $t = 1.5$, the figure shows two-dimensional color maps of the pressure perturbation for a thermally excited specular-wall system at various Knudsen numbers, starting from the ballistic [$\text{Kn} \rightarrow \infty$, Fig. 7(a)] through the continuum-limit [$\text{Kn} = 0.01$, Fig. 7(d)] regime. First, we note that the pressure magnitudes in Fig. 7 are small compared with their counterparts in Fig. 2, where the response to an impulse was considered [cf. Figs. 2(h) and 2(i)]. This is in accordance with the quantitatively weaker Gaussian perturbation considered herein. In agreement with Fig. 6, the free-molecular acoustic field in Fig. 7(a) closely matches with the acoustic pressure in Fig. 7(b) for $\text{Kn} = 1$, for which $t/\text{Kn} = 1.5 \sim O(1)$. However, with decreasing Kn (and increasing t/Kn) to $\text{Kn} = 0.1$ [$t/\text{Kn} = 15$, Fig. 7(c)] and $\text{Kn} = 0.01$ [$t/\text{Kn} = 150$, Fig. 7(d)], the acoustic field departs from its ballistic counterpart. Specifically, the maximum pressure level increases and the effect of molecular diffusion weakens, leading to a more focused signal. This is in line with the results in Figs. 2(a)–2(c), showing the sustaining of the initial impulse singularity at late times in the inviscid limit.

To follow Fig. 7, Fig. 8 inspects the validity of the inviscid ($\text{Kn} \rightarrow 0$) solution derived in Sec. IV. The figure compares between the ideal-flow acoustic pressure calculated at time $t = 1.5$ and the

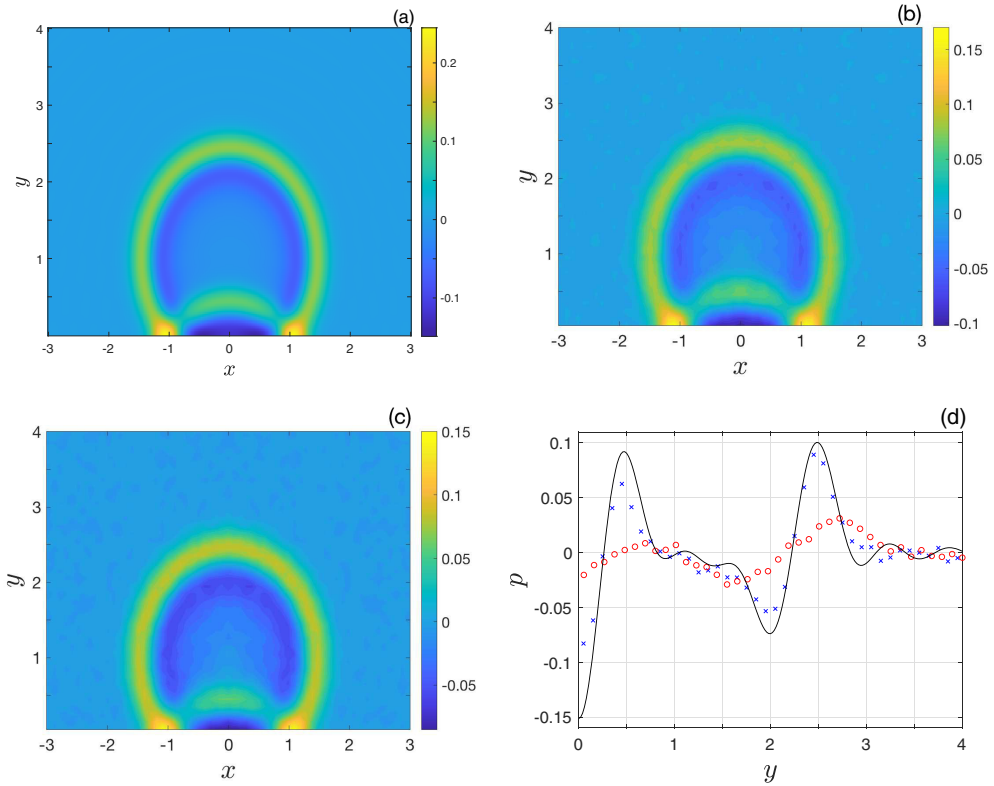


FIG. 8. Comparison between the ideal-flow [$\text{Kn} \rightarrow 0$ (a)] and $\text{Kn} = 0.001$ DSMC predictions (b), (c) for the acoustic pressure at time $t = 1.5$ in response to a Gaussian temperature excitation of specular (b) and isothermal (c) wall systems. (d) DSMC-calculated y variations of the pressure perturbation at $x = 0$ for an isothermal-wall system with $\text{Kn} = 0.01$ (red circles) and $\text{Kn} = 0.001$ (blue crosses). The solid line presents the counterpart ideal-flow ($\text{Kn} \rightarrow 0$) result.

DSMC-predicted pressure fields at $\text{Kn} = 0.001$ for a temperature-excited system with specular [Fig. 8(b)] and isothermal [Fig. 8(c)] walls. These are supplemented by Fig. 8(d), showing DSMC-calculated y variations of the pressure at $x = 0$ for an isothermal-wall system with $\text{Kn} = 0.01$ (in red circles) and $\text{Kn} = 0.001$ (blue crosses), compared with the counterpart inviscid signal (solid line). We first observe the close resemblance of the inviscid and $\text{Kn} = 0.001$ fields in Figs. 8(a)–8(c), indicating the convergence of the numerical DSMC solution to the ideal flow result at small Kn . The peak pressure level is yet largest in Fig. 8(a), where the effect of molecular diffusion vanishes. The convergence is further approved by Fig. 8(d), illustrating the sharpening of the signal peaks with decreasing Kn , varying between the $\text{Kn} = 0.01$ result and the $\text{Kn} \rightarrow 0$ solid-line asymptote. In line with the differences between specular- and isothermal-wall systems discussed in Fig. 4, the pressure levels in the latter are slightly lower. Yet, these overall differences become quantitatively minor at the markedly small Knudsen numbers considered, where the impact of surface impermeability dominates wall thermal conditions. In the vicinity of the $y = 0$ boundary, where the effect of thermal surface conditions is more pronounced, relatively large deviations appear between the ideal and isothermal-wall systems, as seen in Fig. 8(d).

We conclude the discussion of results by considering the acoustic force on the surface in response to a Gaussian excitation. The results follow Eq. (40) for the limit-case calculations, or a momentum balance over the impinging and reflected particles in the DSMC scheme. Figure 9 presents time

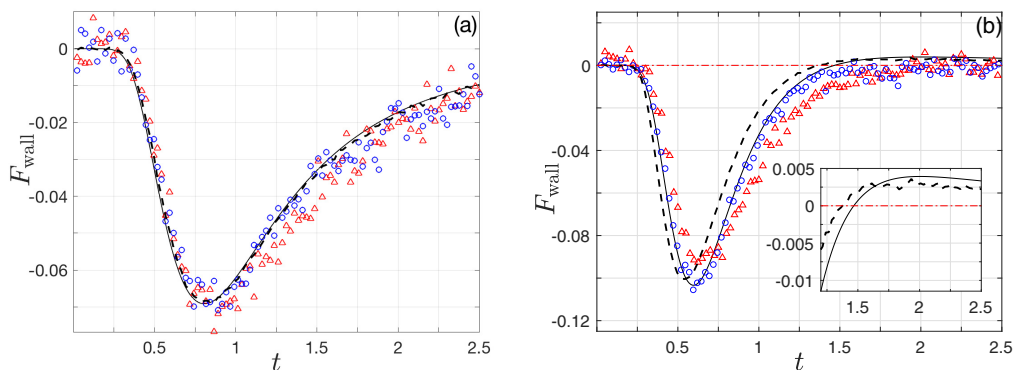


FIG. 9. Time variations of the ε -scaled acoustic force on a specular wall in response to a Gaussian excitation of the density (a) and the temperature (b) fields. The solid lines present the free-molecular result and the blue circles and red triangles show DSMC data at $\text{Kn} = 1$ and 0.1 , respectively. The dashed curves present the free-molecular DSMC-calculated force in a large-amplitude case of $\varepsilon = 1$ [see Eq. (1)] and the dash-dotted red line in (b) highlights $F_{\text{wall}} \equiv 0$, for reference. The inset in (b) is a zoom into the late time force in the linear (solid line) and nonlinear (dashed curve) thermally excited free-molecular systems.

variations of the acoustic force on a specular wall in response to density [Fig. 9(a)] and temperature [Fig. 9(b)] Gaussian excitations. The solid lines show the free-molecular results and the symbols depict counterpart DSMC data at $\text{Kn} = 1$ and 0.1 . Comparing with the results in Fig. 5, the free-molecular force exhibits similar trends to those in the cases of impulse excitations. These include the initial-time vanishing of F_{wall} and the larger repelling force obtained at an earlier time in the temperature-driven compared with the density-driven case. The current Gaussian-excited force is considerably smaller in amplitude than its impulse counterpart, in line with the smaller initial perturbation amplitude. In view of the small-magnitude signal (being ε times smaller before scaling) and the inevitable numerical noise level involved, the agreement between the free-molecular and DSMC predictions at $\text{Kn} = 1$ is very good. At $\text{Kn} = 0.1$, the effect of molecular collisions becomes apparent in the deviation from the free-molecular result at $t \sim O(1)$.

Focusing on the late-time result in the temperature-driven case, we observe that the weak free-molecular attraction force viewed in the impulse-driven system (see Fig. 5) and remanifested in the Gaussian case [see the inset in Fig. 9(b)] is not distinctly captured by DSMC calculations, due to the small amplitude concealed by the numerical noise. To further validate the occurrence of late-time attraction, we carried large-amplitude DSMC computations, where the thermodynamic fields were initially perturbed with nonsmall $\varepsilon = 1$ deviations [see Eq. (1)]. Increasing the initial disturbance amplitude magnified the signal-to-noise ratio, and thus reduced the unwarranted effect of the numerical scatter. The dashed lines in Figs. 9(a) and 9(b) present the free-molecular DSMC-calculated force at $\varepsilon = 1$. Notably, although the linear approximation should be formally invalid at such conditions, the large-amplitude calculation is in qualitative agreement with the ε -scaled linear result in Fig. 9(b). In particular, the DSMC results support the occurrence of a late-time attraction force in a thermally perturbed system at high Knudsen numbers. Additional simulation results with $\varepsilon = 1$ and finite Knudsen numbers (excluded here for brevity) indicate that a late-time positive attraction force persists through $\text{Kn} \gtrsim 1$ and slightly below.

VIII. CONCLUSION

We investigated the effect of gas rarefaction on the propagation and wall reflection of two-dimensional thermodynamic disturbances. Initial system perturbations were modeled as arbitrary (local) small-amplitude density or temperature inhomogeneities, prescribed in the vicinity of an

impermeable specular or diffuse (isothermal) wall. The problem was analyzed in the free-molecular and ideal-flow limits, complemented by DSMC calculations at arbitrary rarefaction rates. Closed-form results were obtained for the collisionless and ideal-flow gas responses to impulse excitations, followed by comparison between DSMC and limit-case predictions for the case of Gaussian perturbations. While the acoustic signal is subject only to a geometric two-dimensional decay and carries to large distances in the inviscid limit, it was found to decay rapidly at high rarefaction rates due to the mechanism of molecular dispersion. Different from the identical gas responses to local compression and heating in the continuum limit, qualitative differences were highlighted and analyzed in the free-molecular regime. The results additionally indicated lower pressure levels in an isothermal- compared with a specular-wall system due to the exchange of gas-surface energy taking place in the former and missing in the latter. The acoustic force acting on the solid surface was studied. Remarkably, apart from an early-time repelling impact, a late-time attraction force was found and rationalized in the case of gas heating excitation at high Knudsen numbers.

The system free-molecular response to local compression differs considerably from its response to heating. In the case of a local density increase, the imposed perturbation leads to an invariantly positive value of the probability density perturbation function, as its initial value is uniformly proportional to the gas density at all molecular speeds [see Eq. (6) with $T_{\text{in}} = 0$]. This changes qualitatively in the case of gas heating, where the initial gas state contains more particles with higher velocities (corresponding to a positive value of the probability perturbation function) and a fewer number of slower molecules [reflected by a negative value of the probability perturbation function; see Eq. (6) with $\rho_{\text{in}} = 0$ and the discussion leading to Eq. (46)]. Consequently, fundamentally different system responses are obtained in the two cases at high Knudsen numbers, for both the hydrodynamic fields and acoustic force variations. In particular, the occurrence of the late-time positive attraction force in the case of gas heating (missing for a density pulse) is directly related to the smaller number of slower particles mentioned above, as rationalized at the end of Sec. VIC.

Advantageously, the DSMC method could be applied in the present paper up to markedly low rarefaction rates, capturing the entire transition and convergence of the numerical solution to the inviscid flow limit. This replaced the utilization of near-continuum schemes, such as the NSF and higher order hydrodynamic models, that should have been employed numerically in the current two-dimensional unsteady setup. A desired extension of the present paper would be an analysis of the two-dimensional scattering of a local source about a finite-length surface, where the effects of structure edges should be examined. This constitutes a topic of a work underway. An additional extension would be the investigation of the counterpart nonlinear problem, where large initial deviations from equilibrium are considered.

APPENDIX A: ACOUSTIC FIELD IN THE FREE-MOLECULAR LIMIT

In terms of the probability perturbation function $\phi(t, x, y, \xi)$ introduced in Eq. (3), the free-molecular ε -scaled acoustic density, tangential and normal velocities, and normal stress components are given by the linearized velocity-space quadratures [32]

$$\begin{aligned}
 \rho(t, x, y) &= \pi^{-3/2} \int_{-\infty}^{\infty} \phi e^{-\xi^2} d\xi, \\
 u(t, x, y) &= \pi^{-3/2} \int_{-\infty}^{\infty} \xi_x \phi e^{-\xi^2} d\xi, \quad v(t, x, y) = \pi^{-3/2} \int_{-\infty}^{\infty} \xi_y \phi e^{-\xi^2} d\xi, \\
 P_{xx}(t, x, y) &= \pi^{-3/2} \int_{-\infty}^{\infty} \xi_x^2 \phi e^{-\xi^2} d\xi, \quad P_{yy}(t, x, y) = \pi^{-3/2} \int_{-\infty}^{\infty} \xi_y^2 \phi e^{-\xi^2} d\xi \quad \text{and} \\
 P_{zz}(t, x, y) &= \pi^{-3/2} \int_{-\infty}^{\infty} \xi_z^2 \phi e^{-\xi^2} d\xi,
 \end{aligned} \tag{A1}$$

respectively, where $d\boldsymbol{\xi} = d\xi_x d\xi_y d\xi_z$. In Appendices A 1 and A 2, specific expressions follow for the cases of isothermal- and specular-wall systems, respectively.

1. Isothermal-wall system

Substituting Eq. (9) for $\phi = \phi^{(\text{iso})}(t, x, y, \boldsymbol{\xi})$ into Eq. (A1) and integrating with ξ_z , we denote

$$\begin{aligned}
I_{m,n}(t, x, y) &= \frac{1}{\pi t^2} \int_0^\infty \left(\frac{y-q}{t}\right)^m \exp\left[-\left(\frac{y-q}{t}\right)^2\right] \int_{-\infty}^\infty \left(\frac{x-s}{t}\right)^n \exp\left[-\left(\frac{x-s}{t}\right)^2\right] \\
&\quad \times \left[\rho_{\text{in}}(s, q) + T_{\text{in}}(s, q) \left(\left(\frac{x-s}{t}\right)^2 + \left(\frac{y-q}{t}\right)^2 - 1 \right) \right] dsdq \quad \text{and} \\
J_{m,n}(t, x, y) &= \frac{y^{m+1}}{\pi} \int_0^t \frac{1}{(t-q)^{m+3}} \exp\left[-\left(\frac{y-q}{t}\right)^2\right] \int_{-\infty}^\infty \left(\frac{x-s}{t-q}\right)^n \exp\left[-\left(\frac{x-s}{t-q}\right)^2\right] \\
&\quad \times \rho_w(q, s) dsdq. \tag{A2}
\end{aligned}$$

In terms of the above notations, we find

$$\begin{aligned}
\rho^{(\text{iso})} &= I_{0,0} + J_{0,0}, \quad u^{(\text{iso})} = I_{0,1} + J_{0,1}, \quad v^{(\text{iso})} = I_{1,0} + J_{1,0}, \quad P_{xx}^{(\text{iso})} = I_{0,2} + J_{0,2} \quad \text{and} \\
P_{yy}^{(\text{iso})} &= I_{2,0} + J_{2,0}. \tag{A3}
\end{aligned}$$

The normal-to-plane stress component is given by

$$\begin{aligned}
P_{zz}^{(\text{iso})} &= \frac{1}{2\pi t^2} \int_0^\infty \exp\left[-\left(\frac{y-q}{t}\right)^2\right] \int_{-\infty}^\infty \exp\left[-\left(\frac{x-s}{t}\right)^2\right] \\
&\quad \times \left[\rho_{\text{in}}(s, q) + T_{\text{in}}(s, q) \left(\left(\frac{x-s}{t}\right)^2 + \left(\frac{y-q}{t}\right)^2 \right) \right] dsdq + \frac{1}{2} J_{0,0}. \tag{A4}
\end{aligned}$$

2. Infinite plane system

Substituting Eq. (13) for $\phi = \phi^{(\text{no-wall})}(t, x, y, \boldsymbol{\xi})$ into Eq. (A1) and integrating with ξ_z , we denote

$$\begin{aligned}
K_{m,n}(t, x, y) &= \frac{1}{\pi t^{m+n+2}} \int_{-\infty}^\infty (y-q)^m \exp\left[-\left(\frac{y-q}{t}\right)^2\right] \int_{-\infty}^\infty (x-s)^n \exp\left[-\left(\frac{x-s}{t}\right)^2\right] \\
&\quad \times \left[\rho_{\text{in}}(s, q) + T_{\text{in}}(s, q) \left(\left(\frac{x-s}{t}\right)^2 + \left(\frac{y-q}{t}\right)^2 - 1 \right) \right] dsdq. \tag{A5}
\end{aligned}$$

In terms of $K_{m,n}$, we write

$$\rho^{(\text{no-wall})} = K_{0,0}, \quad u^{(\text{no-wall})} = K_{0,1}, \quad v^{(\text{no-wall})} = K_{1,0}, \quad P_{xx}^{(\text{no-wall})} = K_{0,2} \quad \text{and} \quad P_{yy}^{(\text{no-wall})} = K_{2,0}. \tag{A6}$$

The normal-to-plane stress component is given by

$$\begin{aligned}
P_{zz}^{(\text{no-wall})} &= \frac{1}{2\pi t^2} \int_{-\infty}^\infty \exp\left[-\left(\frac{y-q}{t}\right)^2\right] \int_{-\infty}^\infty \exp\left[-\left(\frac{x-s}{t}\right)^2\right] \\
&\quad \times \left[\rho_{\text{in}}(s, q) + T_{\text{in}}(s, q) \left(\left(\frac{x-s}{t}\right)^2 + \left(\frac{y-q}{t}\right)^2 \right) \right] dsdq. \tag{A7}
\end{aligned}$$

APPENDIX B: FREE-MOLECULAR HYDRODYNAMIC FIELDS FOR AN IMPULSE-EXCITED ISOTHERMAL-WALL SYSTEM

Substituting Eqs. (28) into Eqs. (A3) and (A4) and making the changes of variables $s = x - y\xi_x/\xi_y$ and $q = t - y/\xi_y$, we denote

$$\begin{aligned} \Phi_{m,n}^{(\delta_\rho)}(t, x, y) &= \frac{x^n(y-1)^m}{\pi t^{2+m+n}} \exp \left[-\left(\frac{x}{t}\right)^2 - \left(\frac{y-1}{t}\right)^2 \right] + \frac{y^{1+m}}{\pi} \int_0^t \frac{1}{(t-q)^{3+m}} \\ &\times \exp \left[-\left(\frac{y}{t-q}\right)^2 \right] \int_{-\infty}^{\infty} \left(\frac{x-s}{t-q}\right)^n \exp \left[-\left(\frac{x-s}{t-q}\right)^2 \right] \rho_w^{(\delta_\rho)}(q, s) ds dq \quad (\text{B1}) \end{aligned}$$

and

$$\begin{aligned} \Phi_{m,n}^{(\delta_T)}(t, x, y) &= \frac{x^n(y-1)^m}{\pi t^{2+m+n}} \left[\left(\frac{x}{t}\right)^2 + \left(\frac{y-1}{t}\right)^2 - 1 \right] \exp \left[-\left(\frac{x}{t}\right)^2 - \left(\frac{y-1}{t}\right)^2 \right] \\ &+ \frac{y^{1+m}}{\pi} \int_0^t \frac{1}{(t-q)^{3+m}} \exp \left[-\left(\frac{y}{t-q}\right)^2 \right] \int_{-\infty}^{\infty} \left(\frac{x-s}{t-q}\right)^n \exp \left[-\left(\frac{x-s}{t-q}\right)^2 \right] \\ &\times \rho_w^{(\delta_T)}(q, s) ds dq, \quad (\text{B2}) \end{aligned}$$

where [see Eq. (11) together with Eqs. (28)]

$$\begin{aligned} \rho_w^{(\delta_\rho)}(t, x) &= \frac{2}{\sqrt{\pi}t^3} \exp \left[-\left(\frac{1}{t}\right)^2 - \left(\frac{x}{t}\right)^2 \right] \quad \text{and} \\ \rho_w^{(\delta_T)}(t, x) &= \frac{2}{\sqrt{\pi}t^3} \left[\left(\frac{x}{t}\right)^2 + \left(\frac{1}{t}\right)^2 - 1 \right] \exp \left[-\left(\frac{1}{t}\right)^2 - \left(\frac{x}{t}\right)^2 \right]. \quad (\text{B3}) \end{aligned}$$

By means of $\Phi_{m,n}^{(\delta_\rho)}(t, x, y)$, we then obtain

$$\begin{aligned} \rho_{\text{FM}}^{(\delta_\rho, \text{iso})} &= \Phi_{0,0}^{(\delta_\rho)}, \quad u_{\text{FM}}^{(\delta_\rho, \text{iso})} = \Phi_{0,1}^{(\delta_\rho)}, \quad v_{\text{FM}}^{(\delta_\rho, \text{iso})} = \Phi_{1,0}^{(\delta_\rho)}, \\ P_{xx, \text{FM}}^{(\delta_\rho, \text{iso})} &= \Phi_{0,2}^{(\delta_\rho)}, \quad P_{yy, \text{FM}}^{(\delta_\rho, \text{iso})} = \Phi_{2,0}^{(\delta_\rho)} \quad \text{and} \quad P_{zz, \text{FM}}^{(\delta_\rho, \text{iso})} = \Phi_{0,0}^{(\delta_\rho)}/2 \quad (\text{B4}) \end{aligned}$$

for the free-molecular hydrodynamic perturbations in response to a density impulse in an isothermal-wall system. Counterpart expressions for the hydrodynamic fields in the case of a heating impulse are obtained by replacing the δ_ρ superscripts in Eqs. (B4) with δ_T .

-
- [1] A. D. Pierce, *Acoustics* (Springer, Cham, 2019).
 [2] L. Sirovich and J. K. Thurber, Propagation of forced sound waves in rarefied gas dynamics, *J. Acoust. Soc. Am.* **37**, 329 (1965).
 [3] G. Maidanik, H. L. Fox, and M. Heckl, Propagation and reflection of sound in rarefied gases. I. Theoretical, *Phys. Fluids* **8**, 259 (1965).
 [4] S. K. Loyalka and T. C. Cheng, Sound-wave propagation in a rarefied gas, *Phys. Fluids* **22**, 830 (1979).
 [5] S. Stefanov, P. Gospodinov, and C. Cercignani, Monte Carlo simulation and Navier-Stokes finite difference calculation of unsteady-state rarefied gas flows, *Phys. Fluids* **10**, 289 (1998).
 [6] F. Sharipov and D. Kalempa, Oscillatory Couette flow at arbitrary oscillation frequency over the whole range of the Knudsen number, *Microfluid. Nanofluid.* **4**, 363 (2008).

- [7] D. Kalempa and F. Sharipov, Sound propagation through a rarefied gas confined between source and receptor at arbitrary Knudsen number and sound frequency, *Phys. Fluids* **21**, 103601 (2009).
- [8] H. Struchtrup, Resonance in rarefied gases, *Continuum Mech. Thermodyn.* **24**, 361 (2012).
- [9] D. Kalempa and F. Sharipov, Sound propagation through a rarefied gas. influence of the gas-surface interaction, *Int. J. Heat Fluid Flow* **38**, 190 (2012).
- [10] T. Tsuji and A. Aoki, Moving boundary problems for a rarefied gas: Spatially one- dimensional case, *J. Comput. Phys.* **250**, 574 (2013).
- [11] A. Manela and N. G. Hadjiconstantinou, On the motion induced in a gas confined in a small-scale gap due to instantaneous boundary heating, *J. Fluid Mech.* **593**, 453 (2007).
- [12] A. Manela and N. G. Hadjiconstantinou, Gas-flow animation by unsteady heating in a microchannel, *Phys. Fluids* **22**, 062001 (2010).
- [13] A. Manela, G. A. Radtke, and L. Pogorelyuk, On the damping effect of gas rarefaction on propagation of acoustic waves in a microchannel, *Phys. Fluids* **26**, 032001 (2014).
- [14] Y. Ben-Ami and A. Manela, Acoustic wave propagation at non-adiabatic conditions: The continuum limit of a thin acoustic layer, *Phys. Rev. Fluids* **5**, 033401 (2020).
- [15] A. Manela and Y. Ben-Ami, Propagation of two-dimensional vibroacoustic disturbances in a rarefied gas, *Phys. Rev. Fluids* **6**, 093401 (2021).
- [16] N. G. Hadjiconstantinou and A. L. Garcia, Molecular simulations of sound wave propagation in simple gases, *Phys. Fluids* **13**, 1040 (2001).
- [17] N. G. Hadjiconstantinou, Sound wave propagation in transition-regime micro- and nanochannels, *Phys. Fluids* **14**, 802 (2002).
- [18] N. G. Hadjiconstantinou and O. Simek, Sound propagation at small scales under continuum and non-continuum transport, *J. Fluid Mech.* **488**, 399 (2003).
- [19] A. D. Hanford, P. D. O'Connor, J. B. Anderson, and L. N. Long, Predicting absorption and dispersion in acoustics by direct simulation Monte Carlo: Quantum and classical models for molecular relaxation, *J. Acoust. Soc. Am.* **123**, 4118 (2008).
- [20] L. Wu, Sound propagation through a rarefied gas in rectangular channels, *Phys. Rev. E* **94**, 053110 (2016).
- [21] X. Liu, X. Chi, Q. Guo, and J. Yang, Study of acoustic wave propagation in micro- and nano channels, *Wave Motion* **76**, 51 (2018).
- [22] A. Manela and Y. Ben-Ami, Non-continuum effects on a squeezed gas film in a two-dimensional acoustic resonator, *J. Fluid Mech.* **946**, A38 (2022).
- [23] G. Chen, Ballistic-diffusive equations for transient heat conduction from nano to macro scales, *J. Heat Transfer* **124**, 320 (2002).
- [24] D. Y. Tzou, *Macro- to Microscale Heat Transfer* (Wiley, Chichester, UK, 2015).
- [25] D. Y. Tzou and E. J. Pfautsch, Ultrafast heating and thermomechanical coupling induced by femtosecond lasers, *J. Heat Transfer* **124**, 284 (2002).
- [26] J. G. Logan, Propagation of thermal disturbances in rarefied gas flows, *AIAA J.* **1**, 699 (1963).
- [27] B. M. Berkovsky and V. G. Bashtovoi, The finite velocity of heat propagation from the viewpoint of the kinetic theory, *Int. J. Heat Mass Transf.* **20**, 621 (1977).
- [28] B. Zappoli and D. Bailly, Transport in confined compressible fluid under time-dependent volumetric heat sources, *Phys. Fluids* **2**, 1771 (1990).
- [29] A. Herczynski and D. R. Kassoy, Response of a confined gas to volumetric heating in the absence of gravity. I: Slow transients, *Phys. Fluids* **3**, 566 (1991).
- [30] A. L. Danforth and L. N. Long, Nonlinear acoustic simulations using direct simulation Monte Carlo, *J. Acoust. Soc. Am.* **116**, 1948 (2004).
- [31] Y. Ben-Ami and A. Manela, The effect of a solid boundary on the propagation of thermodynamic disturbances in a rarefied gas, *Phys. Fluids* **32**, 092002 (2020).
- [32] Y. Sone, *Molecular Gas Dynamics: Theory, Techniques, and Applications* (Birkhäuser, Boston, 2007).
- [33] M. N. Kogan, *Rarefied Gas Dynamics* (Plenum, New York, 1969).
- [34] G. Bird, *Molecular Gas Dynamics and the Direct Simulation of Gas Flows* (Clarendon, Oxford, 1994).
- [35] I. S. Gradshteyn and I. M. Ryzhik, *Table of Integrals, Series, and Products*, 8th ed. (Elsevier, New York, 2014).